Computers and Fluids 164 (2018) 2–11

Contents lists available at ScienceDirect

Computers and Fluids

journal homepage: www.elsevier.com/locate/compfluid

Study of thermal contact resistance of rough surfaces based on the practical topography

Jian-Jun Gou[a], Xing-Jie Ren[a], Yan-Jun Dai[a], Shuguang Li[b], Wen-Quan Tao[a,*]

[a] Key Laboratory of Thermo-Fluid Science and Engineering, Ministry of Education, School of Energy & Power Engineering, Xi'an Jiaotong University, Shaanxi 710049, China

[b] Faculty of Engineering, University of Nottingham, Nottingham NG7 2RD, UK

ARTICLE INFO

Article history:
Received 3 February 2016
Revised 25 May 2016
Accepted 22 September 2016
Available online 23 September 2016

Keyword:
Thermal contact resistance
Rough surfaces
Numerical simulation
Practical topography

ABSTRACT

An approach is proposed to predict the thermal contact resistance (TCR) of rough surfaces. The practical rough topography of surfaces is measured by a contour profiler and is reconstructed to numerically analyze the mechanical and thermal contact performance. The studied material pairs are Ti-6Al-4V—Ti-6Al-4V and C/C-SiC—high temperature ceramic (HTC). The TCR with air gap and vacuum gap conditions are calculated. The approach is validated by the comparison with experimental results of surfaces with the same topography at the same temperatures and loading pressures. The influence of thermal contact conductance between real contact asperities on the TCR of rough surfaces is studied. The approach can be used to predict TCR of different materials with different gap medium under different temperatures and loading pressures. The results show that the real contact area increases approximate linearly, while TCR decreases with the increasing pressure.

1. Introduction

The measurement and prediction of thermal contact resistance between engineering rough surfaces are very essential for a precise thermal management. During the past decades, a lot of researches about experimental measurements [1,2], theoretical [3,4] and numerical [5–7] predictions have been carried out to study TCR.

For the experimental measurement of TCR, methods based on both steady-state [1,2,8–12] and transient [13] heat flux can be found in literatures. Madhusudana [2] analyzed the heat loss in TCR measurement and proposed some suggestions to control the uncertainty in experiments like a shield which can considerably reduce the heat loss. Typically, the influence of vacuum [8] and atmosphere condition [12,14], high temperature (higher than 500 °C) [10] and low temperature(lower than −173 °C) [11] are widely studied.

The prediction of TCR has three key steps: the generation of rough surfaces, the contact deformation analysis and the heat transfer calculation. The rough surfaces should be generated or reconstructed first. The generation of surface roughness can be realized by the statistical parameters like the mean and root-mean-square of roughness [15–17] or its fractal characteristics [18,19]. However, too many assumptions adopted by these methods greatly weaken the reliability of TCR prediction models, and thus it would be a better way to form rough surface models based on the measured real surface topography.

Based on the generated rough surfaces, the contact deformation analysis can then be conducted. Three states of deformation, i.e. fully elastic, elastic-plastic and fully plastic deformation may occur during the contact and this makes the contact mechanics a very complicated topic. Greenwood and Williamson [20] proposed a G-W model to describe the elastic deformation between rough surface and rigid flat surface. Cooper et al. [3] established a fully plastic deformation model to study the TCR between stainless steel and Al. Kogut and Etsion [21] presented a finite element model to analyze the contact performance including the elastic-plastic deformation between a sphere and a rigid flat. In general these excellent works have the objective of obtaining the relationships of the real contact status (real contact spot numbers, sizes, distributions, etc.) with the loading pressure and surface characteristics.

With the real contact status obtained from the deformation analysis, TCR can be acquired by calculating heat transfer problems. Two approaches can be used to calculate TCR of rough surfaces. The first one is based on the analysis of a single contact spot and the related statistical analysis of the whole surface. For instance, the TCR model of a single contact spot proposed by Cooper et al. [3] is widely used by other researchers [4,22,23]. The second approach is to numerically simulate the contact heat transfer of rough surfaces. A multi-scale model of lattice Boltzmann and

* Corresponding author. Fax: +86-29-82669106.
E-mail address: wqtao@mail.xjtu.edu.cn (W.-Q. Tao).

http://dx.doi.org/10.1016/j.compfluid.2016.09.018
0045-7930/

Nomenclature

A	Nominal contact area, [m^2]
E	Elasticity modulus, [GPa]
l_{23}, l_{24}, l_{45}	Length of "2–3", "2–4" and "4–5" segments of specimens, [mm]
P	Pressure, [MPa]
P_m	Measured pressure, [Mpa]
q	Heat flux, [W/m^2]
R_a	Mean absolute deviation of roughness, [μm]
R_q	Standard deviation of roughness, [μm]
T	Temperature, [°C]
TCR	Thermal contact resistance, [$K\,m^2/W$]
$TCCs$	Real constant of element CONTA173, [$W/(K\,m^2)$]
ΔT	Temperature difference, [°C]
u_x, u_y, u_z	Displacement in x, y, z directions, [mm]
x, y, z	Cartesian axis directions, [mm]

finite difference method to conduct the contact thermal analysis of rough surface is reported in [6]. Finite element models of both deformation analysis and the subsequent thermal analysis of rough surfaces are also reported in [24–26].

In this paper, in order to improve the reliability of the TCR prediction model, the rough surfaces of experimental specimens (Ti-6Al-4V—Ti-6Al-4V, HTC—C/C-SiC) are measured by a white light interference microscope, and the coordinates of the roughness are imported to ANSYS to establish a finite element model to conduct the contact deformation and thermal analysis. TCRs of four cases with different temperatures and loading pressures for each material pairs are experimentally measured based on steady state heat flux method.

2. Numerical model

2.1. Computational region

Fig. 1 shows the computational region. The left picture of Fig. 1 displays the schematic specimens of Ti alloy used in the experiment. Each specimen is 48 mm in diameter and 52 mm in height. T_1 –T_6 are temperatures measured by temperature sensors at different locations of the specimens. T_2 and T_5 will be used as the temperature boundary conditions in the numerical simulation. The distances between the temperature sensors and the contact interface are 42, 26, 10, 10, 26, 42 mm, respectively. The cross section of the specimen is a circle. The computational region depicted by the thickest black lines as shown in the right part of Fig. 1 consists of a central inscribed square (34 mm in width) and four around rectangles (20.2 mm in length and 4.7 mm in width). For the around rectangles, the angle between lines of the two outer vertexes to the circle center is about 50° as shown in the figure. This formation enables them to be the largest inscribed rectangles of arches (the green transparent region) between the inscribed square and the circle, and the proving process will not be presented in this work. The height of the computational model is 52 mm.

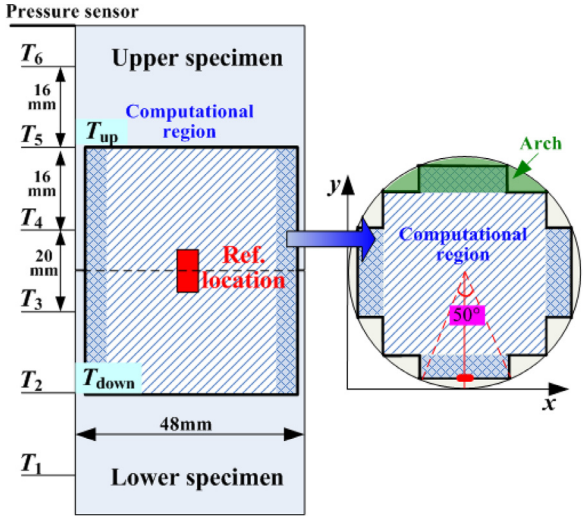

Fig. 1. Computational region.

The loading pressure is measured by a pressure sensor located on the top surface of the upper specimen (see Fig. 1) and is used as the mechanical boundary conditions of the contact analysis. In order to study the influence of the model height on the contact analysis, a model with a height of 84 mm (distance between T_1 and T_6) is also established and the results indicate that the larger model height has very little influence on the numerical results, e.g., the difference of real contact area is less than 0.6% for a loading pressure of 12.08 MPa.

It should also be noted that a reference location as shown in Fig. 1 is marked to ensure the two specimens have the same relative position in the experiment measurement and numerical simulation.

2.2. Rough surfaces

The two rough surfaces are measured by a white light interference microscope (Bruker Contour GT-K 3D Optical Microscope). The measured data with appropriate data processing (only data in computational region is needed) can be imported to ANSYS to reconstruct its geometry. The "keypoints" (KPs) are created first by the input data (x, y, z coordinates), and then non-planar areas (Coons patch) are created by the four adjacent KPs, and the rough surface is finally reconstructed. The sampling length in this work is 0.25 mm. It is clear that a smaller sampling length will present more details of the practical rough surface, however, at the same time it will need more grids and computational time and the increasing costs may make the simulation unable to run. On the other hand, as we all know it is impossible to create a complete model including all the surface details. In this condition what we have done in this work is to establish a model contains as much surface details as possible within our computational ability.

Fig. 2 shows the whole measured surfaces and the geometry reconstructed in ANSYS. Both the upper and the lower specimens are displayed. Fig. 2(a) is the surface of Ti alloy material pair, while Fig. 2(b) is that of C/C-SiC and HTC material pair. The surface geometry in ANSYS is shown in the right part of each figure and the height of the geometry is enlarged 300, 50 and 100 times for Ti alloy, C/C-SiC and HTC specimens, respectively to make the asperities be easily observed. From the figure one can also find that the main features, e.g. valleys of the surface are exhibited in the numerical model. The computational region of each specimen has about 25,000 data points.

The mean absolute deviation (R_a) and standard deviation (R_q) of the roughness of the lower Ti specimen are 2.62 and 3.30 μm, for the upper Ti specimen are 3.01 and 3.79 μm, for the upper C/C-SiC specimen are 15.6 and 23.5 μm, while that for the lower HTC specimen are 10.1 and 13.2 μm, respectively.

2.3. Model formation and meshing

Fig. 3 shows the numerical model. In the figure, A_{up} and A_{low} are the upper boundary plane of the upper specimen and the lower boundary plane of the lower specimen, respectively. A_{up1}

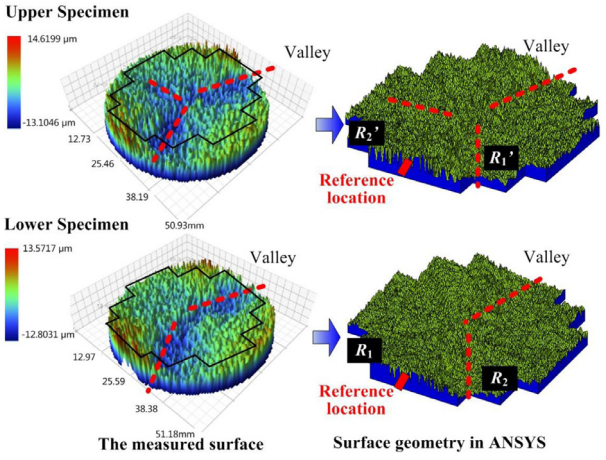

(a) Ti alloy—Ti alloy

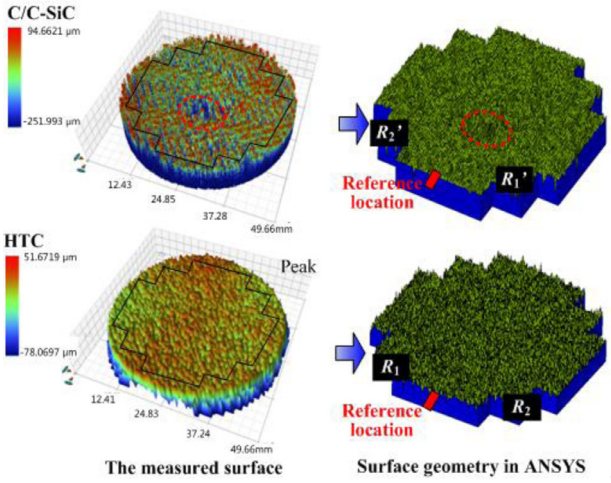

(b) HTC—C/C-SiC

Fig. 2. Lower and upper rough surfaces.

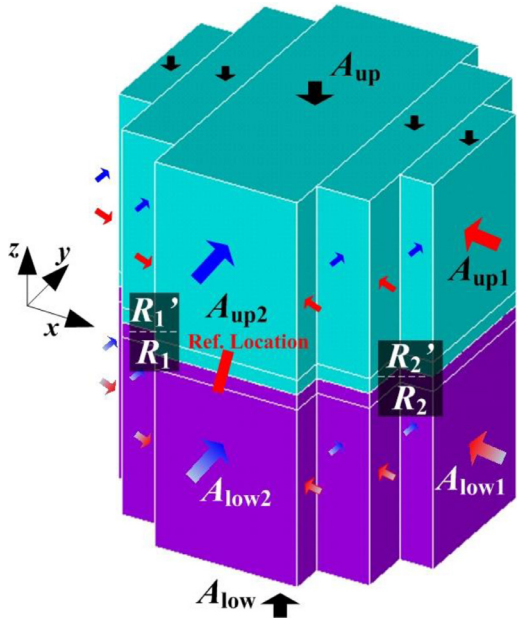

Fig. 3. Numerical model.

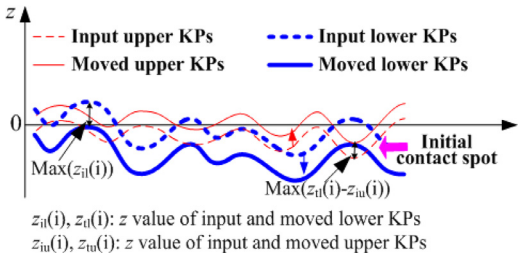

$z_{il}(i)$, $z_{tl}(i)$: z value of input and moved lower KPs
$z_{iu}(i)$, $z_{tu}(i)$: z value of input and moved upper KPs

Fig. 4. Translations of input KPs.

and A_{up2} are profile boundary planes of the upper specimen that perpendicular to the x- and y-axis, respectively, while A_{low1} and A_{low2} are that of the lower specimen, respectively. A_{up1}, A_{up2}, A_{low1} and A_{low2} each indicates a group of planes. One should be very careful with the reconstruction of the rough surfaces to ensure the two surfaces have the same relative position with that of experimental conditions, i.e., typical regions like R_1 and R_2 of the lower surface are corresponding to the R_1' and R_2' regions of the upper surface as shown in Figs. 2 and 3, respectively.

According to the authors' experiences in order to obtain a converged solution the two surfaces should contact with each other at a particular spot (where the contact first occurs during the real contact process) at the initial state. In order to obtain this initial state, the created KPs of the two surfaces by the input data should be translational moved along the height direction as shown in Fig. 4. In the figure, the finer red dashed and solid lines indicate the input and moved lower KPs, while the thicker blue lines indicate that of upper KPs, respectively. $z_{il}(i)$ and $z_{tl}(i)$ denote the z coordinate values of the input and moved lower KPs, respectively, while $z_{iu}(i)$ and $z_{tu}(i)$ denote that of upper KPs. The KPs of the lower surface should be translational moved downward first by $\max(z_{il}(i))$ which is the maximum value of $z_{il}(i)$ and will have a z coordinate value of $z_{tl}(i)$, and then the upper KPs should be translational moved upward by $\max(z_{tl}(i)\text{-}z_{iu}(i))$, and finally we can have the lower and upper KPs with z coordinate values of $z_{tl}(i)$ and $z_{tu}(i)$ as shown in Eq. (1), respectively. With these two translations the two surfaces will contact with each other at a single spot as shown in Fig. 4.

$$\begin{aligned} z_{tl}(i) &= z_{il}(i) - \max(z_{il}(i)) \\ z_{tu}(i) &= z_{iu}(i) + \max(z_{tl}(i) - z_{iu}(i)) \end{aligned} \tag{1}$$

The meshed model is displayed in Fig. 5. The 3D structural solid element SOLID45 with 8 nodes and its corresponding thermal element SOLID70 are used to conduct the mechanical and thermal calculations, respectively. SOLID45 has three degrees of freedom at each node, i.e., translations in x, y and z directions, while SOLID70 has only one degree of freedom (temperature). These solid elements have shape functions for 8-node brick elements as described in [27]. The 3D 4-node surface to surface contact element CONTA173 and target segment element TARGE170 are used to define contact area pairs. The shape function for 3-D 3-node triangular shells without rotational degrees of freedom is adopted by the contact element [27]. The contact elements are located on the surfaces of underlying solid elements and have the same geometric characteristics with the connected surfaces. There are about 4,000,000 elements and 800,000 nodes. The numerical results that are independent of grid numbers are obtained.

It should be noted that for most element types in ANSYS one can find their corresponding element with the same shape functions in other finite element method (FEM) software. Such as SOLID45 and SOLID70 are corresponding to C3D8 and DC3D8 in ABQUS, respectively. Also, the reconstruction process of the rough surfaces is definitely available for other software platform. Therefore, the authors think that the approach presented in this work

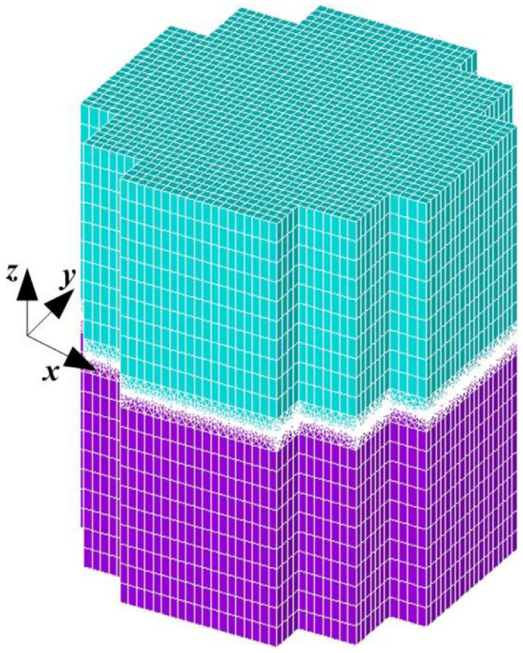

Fig. 5. Meshed model.

could be useful to not only ANSYS users but also those who try to solve TCR problems with FEM.

2.4. Numerical method and boundary conditions

For the mechanical contact problem, the Gauss integration points of contact elements are used as the contact status detection points. The augmented Lagrangian method is used as contact algorithm in which the contact traction (i.e., the Lagrange multiplier) is updated iteratively until a converged result is obtained. The contact convergence criterion is defined by a penetration compatibility value which is assumed to be 0.1 of the depth of underlying elements (i.e., the default value) in this work. A value of less than 0.2 is recommended in ANSYS. A smaller penetration compatibility value means a stricter convergence criterion. If the detected penetration is smaller than the specified value, the contact compatibility is satisfied and the convergence of the contact deformation analysis can then be obtained with other additional converged variables.

On the other hand, for the thermal contact problem, a "real constant" of element CONTA173 is used to consider the thermal contact conductance between two real contact asperities (a more micro scale), i.e., the so-called “TCC”. The detailed information of the “real constant” can be found in [27]. The conductive heat flux transferred between the contacting surfaces is defined by TCC multiply with the temperature difference of the two surfaces. According to the definition, one can notice that a small value of “TCC” means an imperfect thermal contact while a large value means a perfect one. Detailed description can be found in [27]. In order to distinguish the real constant from the thermal contact conductance of the studied rough surfaces, the real constant “TCC” is denoted by TCCs in this work. In this work the thermal contact between real contact asperities is assumed to be perfect and TCCs is assumed to be 1.0×10^{12}. Its influence ($1.0\times10^{7}\sim1.0\times10^{12}$) on TCR of the rough surfaces is also studied and discussed in Section 4.

ANSYS Multiphysics is used to conduct the static contact deformation and thermal analysis. The thermal contact resistance TCR can be calculated by Eq. (2):

$$\mathrm{TCR}=\Delta T/q \tag{2}$$

Table 1
Measured temperatures and loading pressures of experiments.

Material pairs	Case numbers	T_2 (°C)	T_5 (°C)	Loading pressure (MPa)
Ti-6Al-4VTi-6Al-4V	CASE A	197.8	118.0	2.27
	CASE B	205.0	118.8	4.65
	CASE C	208.5	118.5	7.78
	CASE D	210.0	117.7	12.08
C/C-SiC—HTC	CASE A	270.3	151.6	2.903
	CASE B	337.2	181.2	3.489
	CASE C	401.7	210.8	4.09
	CASE D	464.3	238.9	4.614

Table 2
Material properties at room temperature.

Materials	Elastic modulus(GPa)	Poisson's ratio	Yield strength(MPa)
Ti-6Al-4V	120.59	0.286	860
C/C-SiC	60	0.12	860
HTC	420.62	0.165	956

where ΔT is the temperature difference of the average temperature of the two contact interfaces, while q is the heat flux flows through the contact interface. q can be calculated by the heat flow Q, i.e., the sum of the heat flow of each node on the A_{up} or A_{low}, divided by the nominal contact area of the computational region, i.e., the area of A_{up} or A_{low}.

The boundary conditions for the contact deformation analysis can be described as:

$$\begin{aligned}&\text{Lower planes } A_{\mathrm{low}}\text{: } u_x=u_y=u_z=0\\&\text{Upper planes } A_{\mathrm{up}}\text{: } u_x=u_y=0,\ P=Pm\\&\text{Profile planes } A_{\mathrm{low1}} \text{ and } A_{\mathrm{up1}}\text{: } u_x=0\\&\text{Profile planes } A_{\mathrm{low2}} \text{ and } A_{\mathrm{up2}}\text{: } u_y=0\end{aligned} \tag{3}$$

where u_x, u_y, u_z are displacement in x, y, z directions, respectively. P is the pressure in z direction, and P_m is the pressure measured by the pressure sensor. A_{low}, A_{up}..... are boundary planes shown in Fig. 3.

The boundary conditions for the thermal analysis can be described as:

$$\begin{aligned}&\text{Lower planes } A_{\mathrm{low}}\text{: } T=T_2\\&\text{Upper planes } A_{\mathrm{up}}\text{: } T=T_5\\&\text{Profile planes } A_{\mathrm{low1}},A_{\mathrm{low2}},\ A_{\mathrm{up1}} \text{ and } A_{\mathrm{up2}}\text{: } q=0\end{aligned} \tag{4}$$

where T is the temperature, T_2 and T_5 are the temperatures of different locations (see in Fig. 1) measured in the experiment. Four cases (**CASE A, B, C, D**) of TCR for each material pairs are experimentally tested and their corresponding loading pressures and measured T_2 and T_5 are listed in Table 1.

2.5. Material properties

The Ti alloy studied in this work has a chemical composition of Ti-6Al-4V, the C/C-SiC composite is fabricated by an 8-harness woven pierced fabric solidifying with C and SiC matrix, while the HTC is a ZrB_2 based high temperature ceramic. The mechanical and thermal properties of these materials used in the calculations are listed in Tables 2 and 3, respectively. A tangent modulus with a value of 1/100 of elastic modulus is used to describe the bilinear stress-strain curve of the material. The thermal-structural coupling approach used in this paper is the so-called “load transfer method” [27], i.e., the contact deformation is first calculated and the thermal problem is then solved based on the deformed geometry, and thus the temperature influence on the mechanical properties can not be fully considered. At this condition, in the contact analysis of Ti-6Al-4V specimen which has a different mechanical property at different temperatures, the properties at the temperature of

Table 3
Material properties at different temperatures.

	Ti-6Al-4V			C/C-SiC			HTC
T/(°C)	Elastic modulus(GPa)	Poisson's ratio	Thermal conductivity(W/m K)	Axial thermal conductivity(W/m K)	Transverse thermal conductivity(W/m K)	Thermal conductivity(W/m K)
RT	120.59	0.286	6.8	5.2	9.2	93.6
100	120.05	0.284	7.4	6.5	11.3	93.6
200	115.5	0.294	8.7	7.4	12.7	93.6
300	113.39	0.299	9.8	7.7	13.1	93.6
400	/	/	/	7.9	13.3	87.3
500	/	/	/	8.0	13.4	81.1

$(T_2 + T_5)/2$ are used, and this seems to be effective if we consider the small variation of mechanical properties and the possible narrow temperature distribution ranges of $T_5 \sim T_2$: the Elastic Modulus and the Poisson's ratio as shown in Table 3 have a largest fluctuation of 6% and 5% in the temperature range of room temperature (RT)∼300 °C, while the experimental measured T_2 and T_5 as shown in Table 1 has a largest range of 117°∼210° (**CASE D**).

2.6. Heat transfer assumptions

In this work, the air in the gap of the two contact specimens is steady, so the convective heat transfer is not considered, while the air thermal conduction has to be considered. However, ANSYS is unable to simulate the gap medium (between two surfaces, no mesh) thermal conduction directly but can simulate the convective heat transfer between the two surfaces. For the problem studied in this paper, only the temperature and heat flux distributions in the specimens rather than the gap are concerned. In this condition, the heat transferred by gap air conduction can be simulated by the thermal convection between the two contact surfaces: if the heat that transferred by the convection (in simulation) equals to that transferred by air conduction (in real condition), the accurate thermal contact resistance can be obtained. In this paper, the convective heat transfer coefficient is calculated by the thermal conductivity of air divided by the average length of the gap and this ensures the simulated heat transfer (convection) equals to the real heat transfer (conduction). The gap length is calculated by the difference of the average z-coordinates of nodes on the upper and the lower contact interfaces. The thermal conductivities of air at different temperatures are obtained from the appendix of [28]. In addition, one can see that the simulation method discussed above can also be used to calculate other gap medium conduction provided that the medium can be evenly distributed in the gap and brings no extra contact resistance between the studied surfaces.

In this work, the influence of radiative heat transfer between the two contact surfaces is not considered. In fact, one can easily figure out that its influence can be negligible. Take HTC–C/C-SiC material pair under boundary conditions of CASE D as an example, the two surfaces can be assumed to have a surface emissivity of 1 and a radiation view factor of 1. The calculated average temperatures of the lower and upper interface are 443 and 414 °C, respectively. In this condition the radiative heat transfer between the two contact surfaces is about 2271 W/m^2, which is only about 3% of the numerically calculated heat flux flows through the contact interface (68,000 W/m^2). Moreover, the real radiation should have less influence since the surface emissivity and radiation view factor always have a value smaller than 1.

3. Experimental apparatus

The experiment system is shown in Fig. 6. The bottom surface of the lower specimen is heated by a heat source. The pressure can be imposed on the upper plane of the upper specimen provided by a device composed of worms and gears as shown in Fig. 6. A re-circulating cooler and a small heat exchanger made by brass are used to obtain a steady thermal state. Around the specimens are thermal insulation layers to maintain an approximate one-directional heat transfer. The temperatures at each layer locations are measured by thermal couples. The temperature at the two contact surfaces and the heat flux are deduced by the Fourier heat conduction law with the measured temperature T_1 to T_6. The TCR is then calculated by the temperature difference of the two contact interfaces divided by the heat flux as described by Eq. (2). For each measurement the thermal steady state is obtained. TCRs at four cases for each material pairs are measured and the loading pressure and the measured T_2 and T_5 are listed in Table 1.

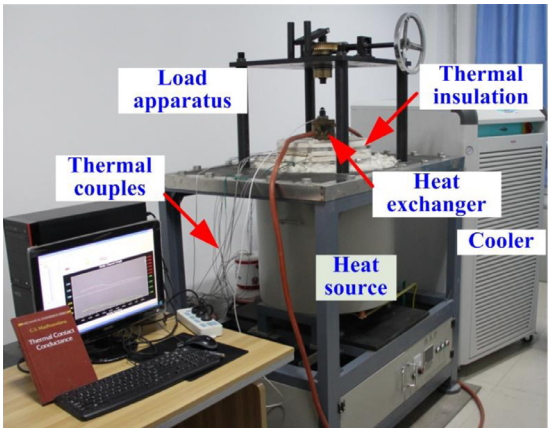

Fig. 6. Experimental apparatus.

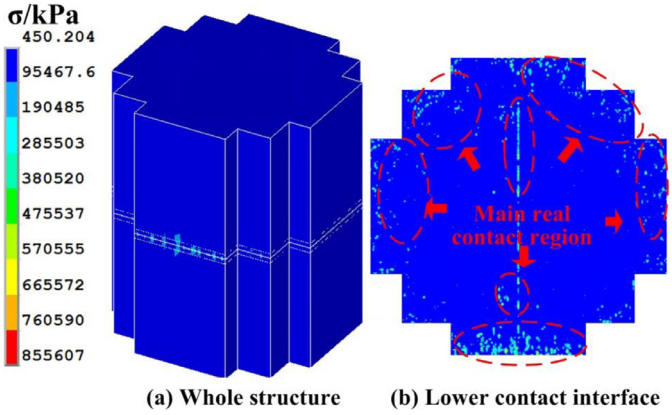

Fig. 7. Stress distribution.

A TCR prediction model should be validated by the comparison with the corresponding experimental measurements at the same conditions including the same surface topography, temperatures, and loading pressures. In this work, as discussed above we can keep the same temperatures and pressures, and almost the same rough surfaces.

4. Results and discussion

The contact deformation and heat transfer characteristics are discussed by the results of Ti alloy material pairs as shown in Sections 4.1 and 4.2.

4.1. Contact analysis

Fig. 7 is the Von Mises stress distribution calculated with boundary conditions of **CASE D** with a loading pressure of 12.08MPa. Figs. 7(a) and (b) show the results of the whole structure and the contact interface of the lower specimen, respectively. The higher stress level can be observed in the region near the real contact spots because the micro roughness leads to this kind of stress concentration. The highest contact stress arises at the contact interface is about 855 MPa. The area-weighted average stress of the real contact area is about 489 MPa. Both values are much greater than the loading pressure 12.08 MPa. On the other hand, the real area of contact is only about 2.1% of the nominal contact area. This means that the real contact only occurs between a few asperity pairs as indicated by red dashed lines in Fig. 7(b). Madhusudana summarized and proposed in [29] that the real contact area of most engineering surface is about 1 to 2% of the nominal

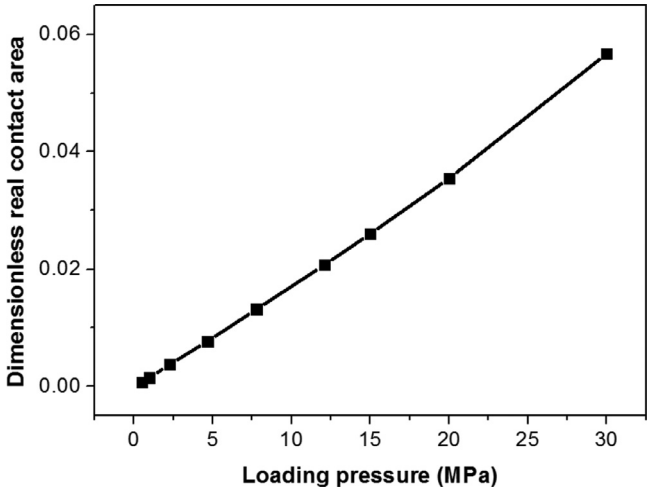

Fig. 8. Real contact area.

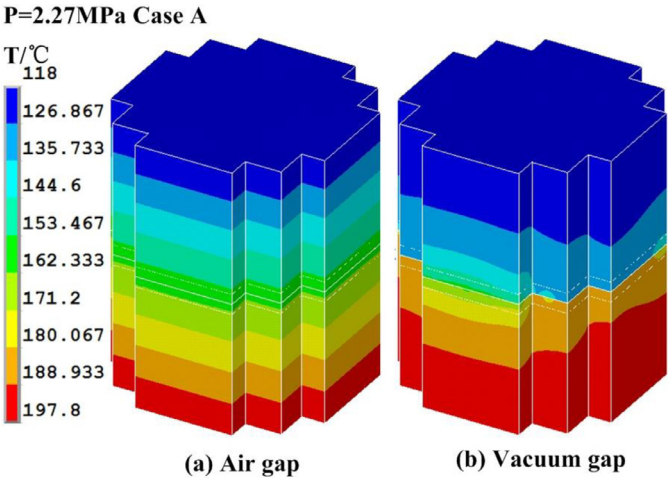

Fig. 9. Temperature distribution.

area under 10 MPa loading pressure. Apparently the real contact area obtained in the mechanical simulation of this work is reasonable.

The main objective of mechanical contact analysis is to determine the real contact area and its distribution. According to many previous works [30,31] we know that the real contact area has an approximate linear relationship with loading pressure. This phenomenon is also revealed by the numerical results of this work as shown in Fig. 8 which displays the dimensionless real contact area of **CASE A** with different loading pressures. The dimensionless real contact area can be calculated by the real contact area divided by the nominal area.

4.2. Thermal analysis

The thermal problems with gap air conduction and the vacuum atmosphere are considered. The temperature distributions of **CASE A** with a loading pressure of 2.27 MPa are shown in Figs. 9 and 10, respectively. Figs. 9 (a) and (b) are the temperature distributions of the whole volumes for conditions of air gap and vacuum gap, respectively. As shown in Fig. 9 the temperature distribution calculated with air conduction is more uniform than that of vacuum. The same phenomenon can be observed at the lower contact interface as shown in Figs. 10(a) and (b). It should be noted that Figs. 10(a) and (b) have different legend spans. The temperature range for Figs. 10(a) and (b) are 158.5 °C∼160.8 °C and

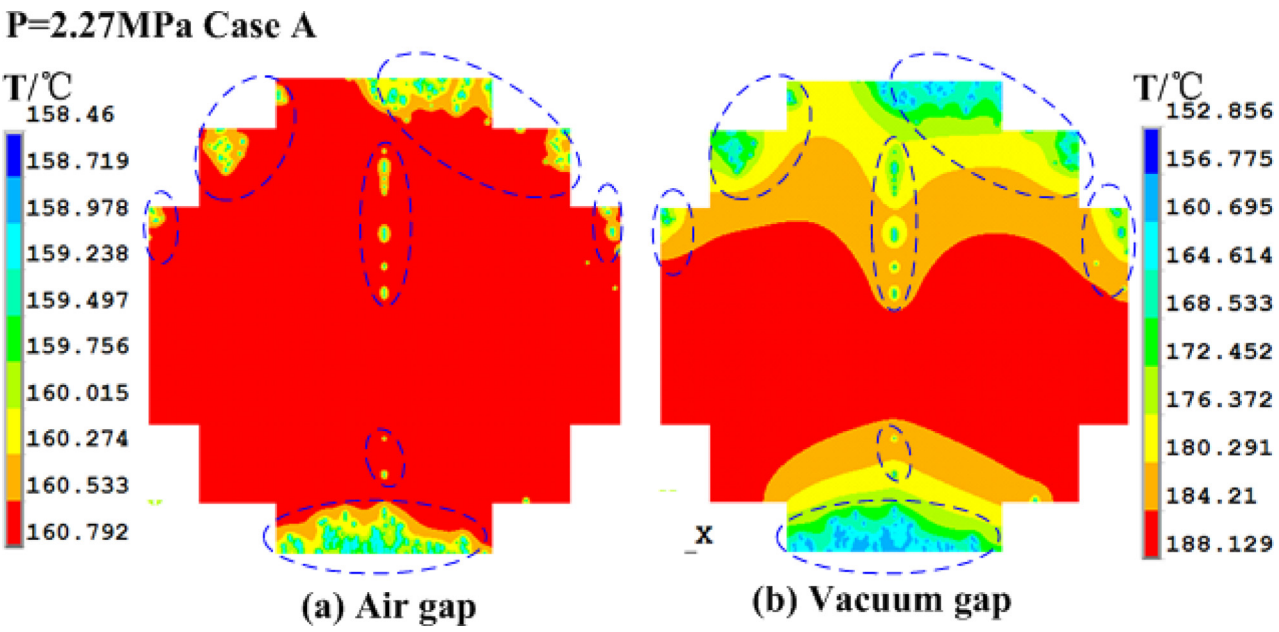

Fig. 10. Temperature distribution of the lower contact interface.

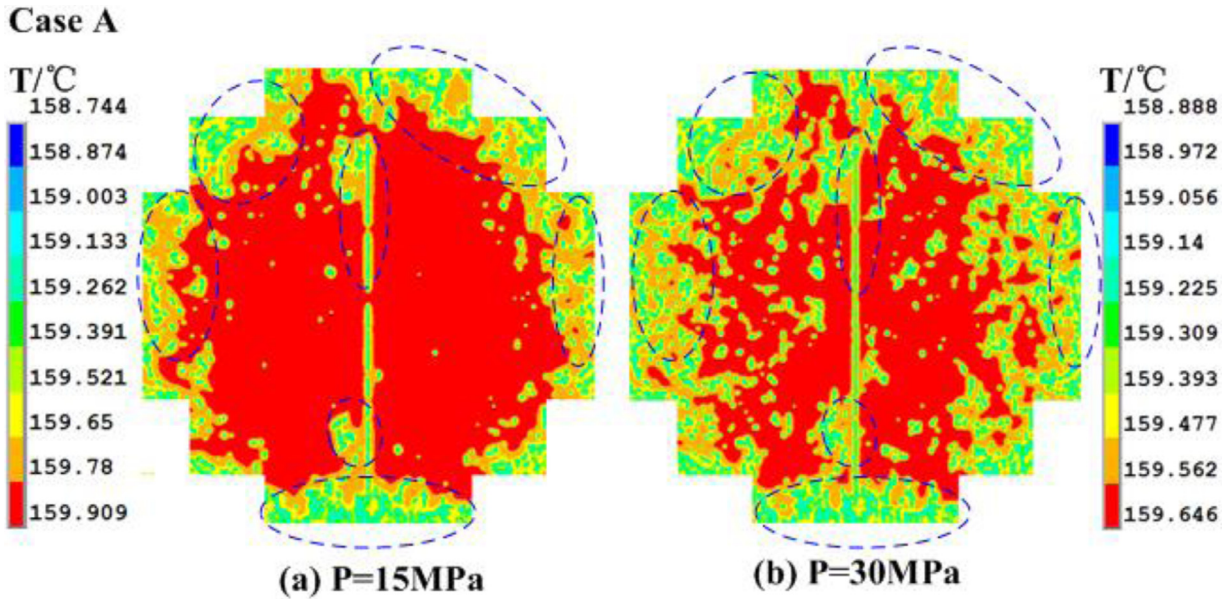

Fig. 11. Temperature distribution of different loading pressures.

152.9 °C∼188.1 °C, respectively. The narrower range strongly indicates a much more uniform temperature distribution. This is obviously due to the gap air conduction which brings about an enhancement of heat transfer between the two specimens.

Generally, the denser temperature contours means the stronger heat transfer. The main real contact region is depicted by blue dashed lines in Fig. 10. As shown in Fig. 10 the denser temperature contours and the lower temperature level can be observed at the area adjacent to the real contact regions. For both air and vacuum atmosphere the heat transfer near the real contact regions is greatly enhanced by the solid thermal conduction.

Figs. 11(a) and (b) show the temperature distribution of the lower contact interface with loading pressures of 15 and 30 MPa, respectively. The gap air conduction is considered in Fig. 11. It is clear that lower temperature area (the real contact area) increases with the increasing loading pressure. The temperature difference of the two contact interfaces (upper and lower) under different pressures are obtained as shown in Fig. 12. The temperature difference decreases and the decreasing trend becomes slower with the increase of pressure. As shown in Figs. 11 and 12, the heat transfer between the two contact specimens is enhanced by the increasing loading pressure and certainly will decrease the thermal contact resistance.

4.3. Stress and temperature distribution of C/C-SiC and HTC pair

For C/C-SiC and HTC material pair, the stress and temperature distribution of the lower contact interface for four cases (see Table 1) are shown in Figs. 13 and 14, respectively. The loading pressure and the calculated real contact area for each case are marked in each figure. With the increasing of loading pressure from 2.903∼4.614 MPa, the real contact area increases from 0.12% to 0.19%. Compare with Ti alloy pair (see Fig. 8), the real contact

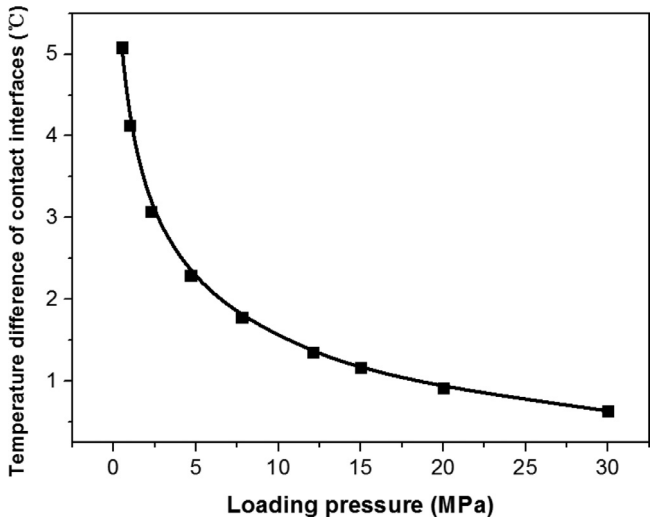

Fig. 12. Temperature difference of contact interfaces.

area of C/C-SiC and HTC material pair has a smaller value and a slower increasing trend. This may be due to the higher elastic modulus of UHT and the lower Poisson's ratio which means a higher shear modulus of the two materials (see Table 2). As shown in Fig. 14, the low temperature area of the contact interface increases with the increasing loading pressure and real contact area.

4.4. Thermal contact resistance

4.4.1. The influence of TCCs and loading pressures

As discussed above, a "real constant" of element CONTA173, i.e., TCCs is used to simulate the thermal contact conductance of real contact asperities. Three values of TCCs, 1.0×10^7, 1.0×10^9 and 1.0×10^{12}, are used in the calculation of Ti alloy material pair to clarify its influence on TCR. In order to save time a smaller computational region $\boldsymbol{A_1}$ as shown in Fig. 15 is selected to do this study. The area of $\boldsymbol{A_1}$ is 1/16 of the inscribed square. The corresponding results of different TCCs values with **CASE A** boundary conditions (different loading pressures) can be seen in Fig. 16 as dashed, short dashed and solid lines, respectively. The enlarged figure in Fig. 16 shows the deviation of the three cases. It can be found that the influence of TCCs on the problem in this work can be negligible with a largest derivation of smaller than 3%. In this paper, the results discussed later have a TCCs value of 1.0×10^{12}. Although as shown in Fig. 16 the influence of TCCs becomes larger while the pressure increases, under a lower pressure which means a smaller real contact area, its influence can be negligible. However, as a matter of fact its influence is also closely related to the material properties and the gap medium properties. So in order to determine an appropriate value of TCCs it would be a better way to conduct some comparison calculations. With an appropriate TCCs value, the approach presented in this work can be applied to a relatively wide range of loading pressures.

Fig. 17 shows the thermal contact resistance obtained by **CASE A** with different loading pressures of Ti alloy pairs. The black line with square symbols is the results of air gap, while the blue line with circle symbols is the results of vacuum gap. In order to display two lines in one figure the log10 type coordinates is used. As shown in the figure the TCR obtained by the vacuum gap is much larger than that of air gap, and the difference decreases from 99% to 84% with the pressure increases from 0.5 to 30 MPa. This is because the heat transferred between real contact asperities plays a more important role under a higher loading pressure which means a larger real contact area. From the two lines one can see that the TCR decreases and the decreasing tendency slows down with the increasing pressure. The TCR with air gap decreases from about 4.3×10^{-4} to 5.2×10^{-5} (K m^2/W), while that of vac-

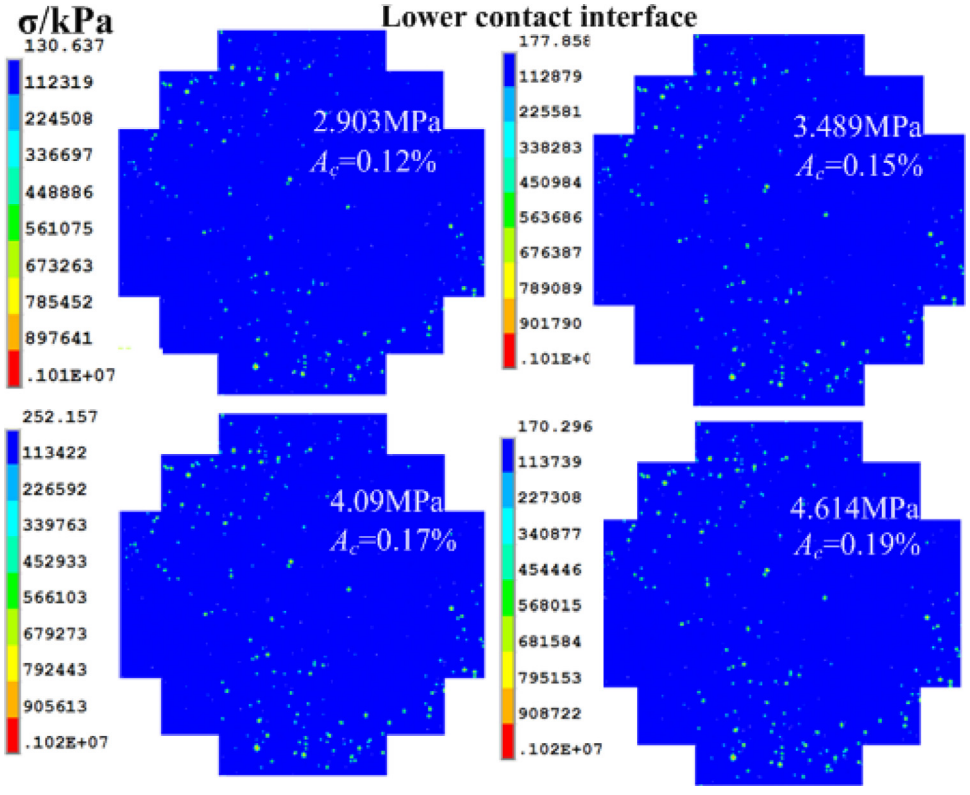

Fig. 13. Stress distribution of lower contact interfaces for HTC—C/C-SiC.

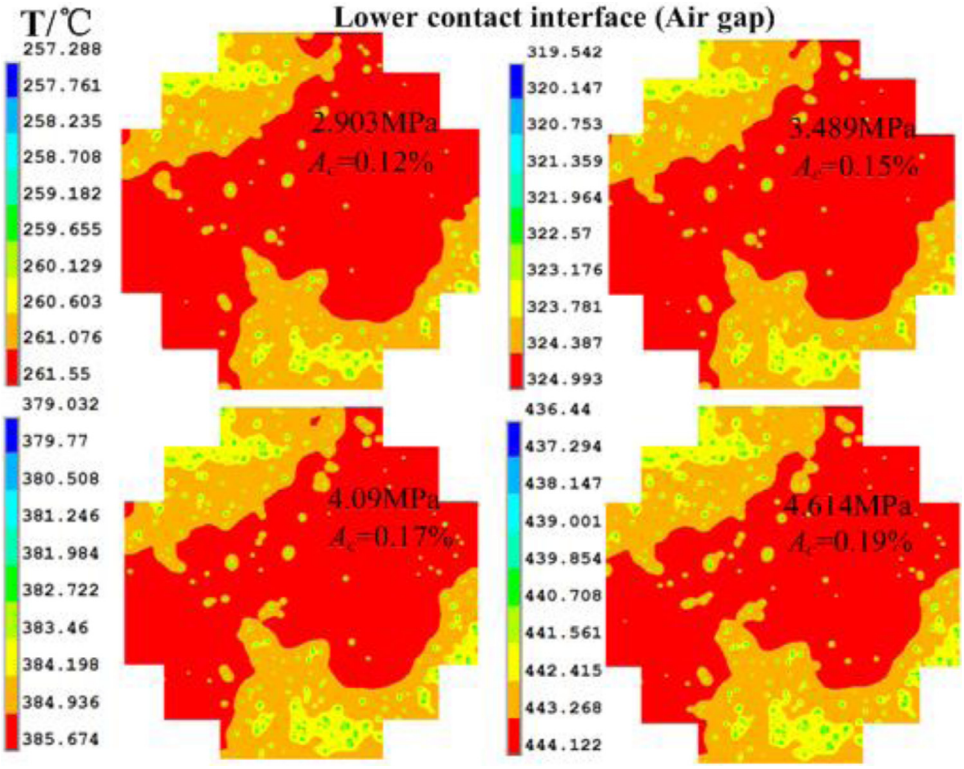

Fig. 14. Temperature distribution of lower contact interfaces for HTC—C/C-SiC.

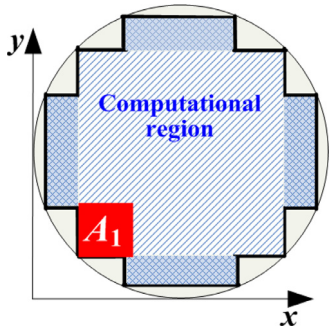

Fig. 15. A smaller computational region.

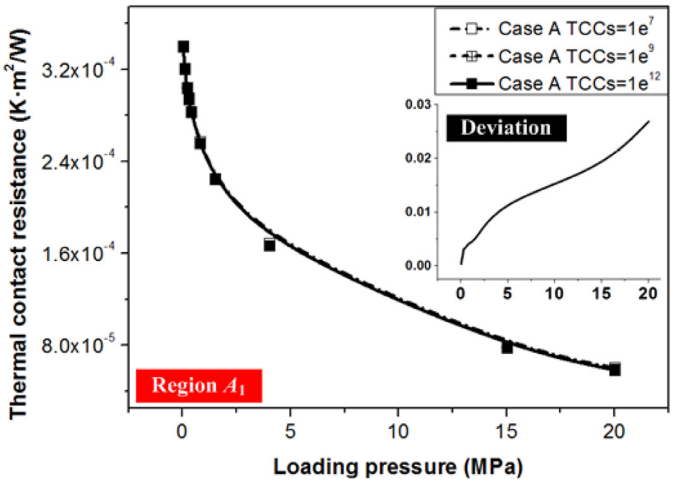

Fig. 16. TCR of the computational region A_1 for Ti alloy pairs.

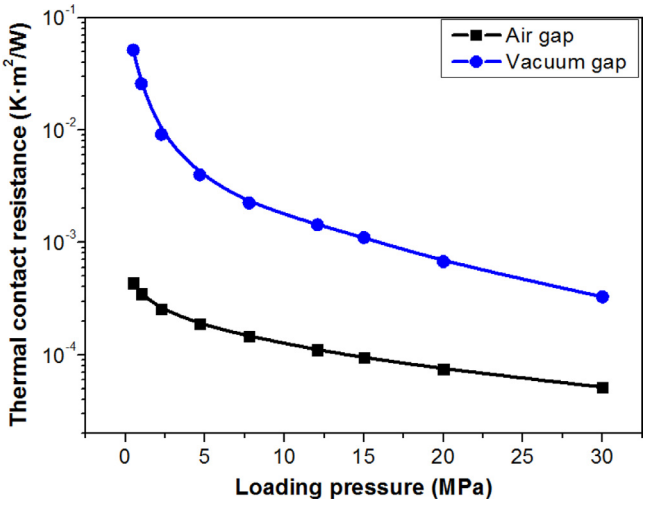

Fig. 17. Thermal contact resistance of Ti alloy pairs.

uum from about 5.1×10^{-2} to 3.3×10^{-4} as the pressure increases from 0.5 to 30 MPa. It is obvious that the TCR with vacuum conditions decreases more quickly which means more sensitive to the loading pressure than air conditions.

4.4.2. The comparison with experimental results

The thermal contact resistance of Ti alloy pairs, and C/C-SiC and HTC pairs for **CASE A, CASE B, CASE C** and **CASE D** are experimentally measured. The measured temperatures and pressures are listed in Table 1. The measured and the calculated TCR are listed in Table 4. As can be found in the table that the experimental and numerical results have a relatively good agreement with a largest difference of 19.4% and 36.9% for Ti-6Al-4V—Ti-6Al-4V and HTC—C/C-SiC, respectively. Considering the complicated mechanism of the contact heat transfer this kind of difference can be acceptable.

Table 4
Measured and the numerically calculated thermal contact resistance.

Material pairs	Case numbers	TCR(*Num.*) (K m^2/W)	TCR (*Exp.*) (K m^2/W)	Difference (%)
Ti-6Al-4V—Ti-6Al-4V	CASE A	0.000255	0.000315	−19.4
	CASE B	0.000187	0.000185	1.08
	CASE C	0.000143	0.000153	−6.5
	CASE D	0.000108	0.000134	−19.4
C/C-SiC—HTC	CASE A	0.000596	0.000762	−21.8
	CASE B	0.000527	0.000568	−7.2
	CASE C	0.00047	0.000405	16.0
	CASE D	0.000427	0.000312	36.9

In addition, the model established in this work has less assumption about the rough topography of the contact surfaces than most of the available literatures and improves the reliability of the proposed approach.

With the enough accuracy and reliability we can conclude that this approach can be used to calculate thermal contact resistance of rough surfaces with different environment conditions (temperature, pressure and gap medium) and surface topography (micrometer-scale). In addition, the medium between the two specimens should have some characteristics: it should be evenly distributed in the gap and there should be no extra contact resistance between the medium and the studied surface.

5. Conclusions

An approach is proposed to predict the thermal contact resistance based on the practical rough surfaces in this work. The rough topography of contact surfaces is measured by a surface profiler and used to establish a numerical model to study the contact mechanical deformation and heat transfer and to finally calculate the thermal contact resistance of rough surfaces with an air gap and a vacuum gap, respectively. Two pairs of materials Ti-6Al-4V—Ti-6Al-4V and HTC—C/C-SiC are studied. The influence of thermal contact conductance between two real contact asperities is analyzed. The approach is validated by a good agreement between the numerical and the experimental results with the same temperature, pressure and surface topography. The numerical results indicate:

1. The proposed approach can be used to predict the thermal contact resistance of micrometer-scale rough surfaces under different temperatures and loading pressures, and different gap mediums provided that it can be evenly distributed in the gap and brings no extra contact resistance between the studied surfaces.
2. The influence of thermal contact conductance between real contact asperities increases with the increasing loading pressure and an appropriate value should be determined by comparison calculations.
3. The thermal contact resistance decreases while the tendency slows down with the increase of the loading pressure. The thermal contact resistance obtained in air condition is much smaller and also less sensitive to the variation of loading pressures than that of vacuum gap condition.

Acknowledgment

This study is supported by the Key Project of International Joint Research of National Nature Science Foundation of China (51320105004).

References

[1] Marotta EE, Fletcher LS. Thermal contact conductance of selected polymeric materials. J Thermophys Heat Transfer 1996;10(2):334–42.
[2] Madhusudana CV. Accuracy in thermal contact conductance experiments - The effect of heat losses to the surroundings. Int Commun Heat Mass Transfer 2000;27(6):877–91.
[3] Cooper MG, Mikic BB, Yovanovich MM. Thermal contact conductance. Int J Heat Mass Transfer 1969;12(3):279–300.
[4] Zou MQ, Yu BM, Cai JC, Xu P. Fractal model for thermal contact conductance. J Heat Transfer-Trans ASME 2008;130(10):101301 (9 pages).
[5] Black AF, Singhal V, Garimella SV. Analysis and prediction of constriction resistance for contact between rough engineering surfaces. J Thermophys Heat Transfer 2004;18(1):30–6.
[6] Cui TF, Li Q, Xuan YM, Zhang P. Multiscale simulation of thermal contact resistance in electronic packaging. Int J Therm Sci 2014;83:16–24.
[7] Verma NN, Mazumder S. Extraction of thermal contact conductance of metal–metal contacts from scale-resolved direct numerical simulation. Int J Heat Mass Transfer 2016;94:164–73.
[8] Ding C, Wang R. Thermal contact conductance of stainless steel-GFRP interface under vacuum environment. Exp Therm Fluid Sci 2012;42(0):1–5.
[9] Zhang P, Xuan Y, Li Q. A high-precision instrumentation of measuring thermal contact resistance using reversible heat flux. Exp Therm Fluid Sci 2014;54(0):204–11.
[10] Liu D, Luo Y, Shang X. Experimental investigation of high temperature thermal contact resistance between high thermal conductivity C/C material and Inconel 600. Int J Heat Mass Transfer 2015;80(0):407–10.
[11] Choi YS, Kim MS. Experiments on thermal contact conductance between metals below 100 K. AIP Conf Proc 2014;1573:1070–7.
[12] Dou R, Ge T, Liu X, Wen Z. Effects of contact pressure, interface temperature, and surface roughness on thermal contact conductance between stainless steel surfaces under atmosphere condition. Int J Heat Mass Transfer 2016;94:156–63.
[13] Chen J, Zhang W, Feng Z, Cai W. Determination of thermal contact conductance between thin metal sheets of battery tabs. Int J Heat Mass Transfer 2014;69(0):473–80.
[14] Wahid SMS, Madhusudana CV. Gap conductance in contact heat transfer. Int J Heat Mass Transfer 2000;43(24):4483–7.
[15] Wu JJ. Simulation of rough surfaces with FFT. Tribol Int 2000;33(1):47–58.
[16] Bakolas V. Numerical generation of arbitrarily oriented non-Gaussian three-dimensional rough surfaces. Wear 2003;254(5-6):546–54.
[17] Wu JJ. Simulation of non-Gaussian surfaces with FFT. Tribol Int 2004;37(4):339–46.
[18] Majumdar A, Tien CL. Fractal characterization and simulation of rough surfaces. Wear 1990;136(2):313–27.
[19] Ganti S, Bhushan B. Generalized fractal analysis and its applications to engineering surfaces. Wear 1995;180(1-2):17–34.
[20] Greenwood JA, Williamson JBP. Contact of nominally flat surfaces. Proc R Soc London Ser A-Math Phys Sci 1966;295(1442):300–19.
[21] Kogut L, Etsion I. Elastic-plastic contact analysis of a sphere and a rigid flat. J Appl MechTrans ASME 2002;69(5).
[22] Zhao JF, Wang AL, Yang CX. Prediction of thermal contact conductance based on the statistics of the roughness profile characteristics. Int J Heat Mass Transfer 2005;48(5):974–85.
[23] Ji C, Zhu H, Jiang W. Fractal prediction model of thermal contact conductance of rough surfaces. Chin J Mech Eng 2013;26(1):128–36.
[24] Murashov MV, Panin SD. Modeling of thermal contact conductance. In: Proceedings of the ASME international heat transfer conference, 6; 2010. p. 387–92.
[25] Thompson MK. A multi-scale iterative approach for finite element modeling of thermal contact resistance. Department of mechanical engineering. Massachusetts Institute of Technology; 2007.
[26] Murashov MV, Panin SD. Numerical modelling of contact heat transfer problem with work hardened rough surfaces. Int J Heat Mass Transfer 2015;90:72–80.
[27] ANSYS 14.5 help.
[28] Yang SM, Tao WQ. Heat transfer. Higher Education Press; 2006.
[29] Madhusudana CV. Thermal contact conductance. Springer; 1995.
[30] Sahoo P, Ghosh N. Finite element contact analysis of fractal surfaces. J Phys D-Appl Phys 2007;40(14):4245–52.
[31] Kucharski S, Starzynski G. Study of contact of rough surfaces: modeling and experiment. Wear 2014;311(1-2):167–79.